Int. J. Solids Structures Vol. 20, No. 8, pp. 747–760, 1984
Printed in the U.S.A.

0020-7683/84 $3.00 + .00
Pergamon Press Ltd.

NONSPECULAR REFLECTION OF BOUNDED ACOUSTIC BEAMS FROM THE LIQUID–SOLID INTERFACE OF TWO ELASTIC LAYERS ON A HALFSPACE UNDER WATER

D. B. BOGY and S. M. GRACEWSKI
Department of Mechanical Engineering, University of California, Berkeley, CA 94720, U.S.A.

(*Received* 24 *January* 1983; *in revised form* 5 *September* 1983)

Abstract—The plane wave reflection coefficient is derived for a layered halfspace with an arbitrary number of layers, and it is compared to previously published results of others. The structure is then specialized to silver and nickel layers on a copper substrate, and the reflection coefficient is studied numerically for changing layer thicknesses and frequency. Dispersion curves for the lowest Rayleigh mode are presented, and the nonspecular reflection of bounded acoustic beams from the water–silver interface is studied.

1. INTRODUCTION

This paper is the third in a series by the authors concerning nonspecular reflection of bounded acoustic beams in water from the liquid–solid interface of layered elastic media. In [1] we derived in closed analytical form the reflection coefficient for a single layer on a dissimilar substrate using linear elasticity theory. We also obtained in that paper the corresponding results for three different approximate models for the thin layer.

In [2] we studied the exact reflection coefficient derived in [1], and we numerically evaluated its modulus for a wide range of material combinations. These included cases previously studied by others, such as the elastic halfspace without layers as well as the single elastic layer submerged in water. A rather extensive list of references to this work is contained in [2] and will not be repeated here. We also studied in [2] the specific examples of the "stiffened" and "loaded" halfspace as distinguished by Farnell and Adler[3] by the relative values of the material constants of the layer and halfspace. The reflection coefficient was studied as a function of the frequency–thickness parameters. In particular, we investigated and explained the stiffening case for values of the frequency–thickness parameter greater than the cut-off value for the propagating Rayleigh mode. This cut-off occurs when the Rayleigh pole in the complex wave number plane reaches the shear wave number (which is a branch point of the reflection coefficient) of the substrate. We found that the mode still exists, in a sense, for frequency–thickness values above the cut-off, but its energy leaks into the substrate. For very high values of this parameter, however, the Rayleigh mode of the layer is approached. This occurs when the frequency–thickness parameter becomes large enough so that the amplitude of the Rayleigh wave for the layer material has essentially decayed to zero at the interface depth.

In the present paper we consider the case of two elastic layers on an elastic halfspace. In certain types of diffusion bonding the need for such a structure arises. The reflection coefficient and the associated nonspecular reflection of bounded acoustic beams in water provide possible avenues for detecting interface flaws in the structure. In Section 2 we consider a single elastic layer (in vacuum) containing a set of longitudinal and transverse plane harmonic waves, and we show that the matrix function relating the velocity and traction at one face to those quantities at its other face is independent of the phase of the waves. It can therefore be applied to each layer in a multilayered halfspace without regard to the position of the layer. This result was implicitly assumed and used in Thomson[4] and Brekhovskikh[5]. We then derive in Section 3 the reflection coefficient for a general multilayered halfspace submerged in a liquid. The result obtained has a different phase from that presented in [4, 5]. The structure is specialized to two layers in Section 4, and the particular case of silver on nickel on copper is studied. Numerical results are presented for the modulus of the reflection coefficient for various thickness ratios of the two layers

and various values of frequency–thickness parameters. Also the lowest Rayleigh mode pole is obtained as a function of these parameters. Finally, beam profiles are calculated for the nonspecular reflection of bounded beams in water.

2. VELOCITY-TRACTION TRANSFER MATRIX FOR SINGLE LAYER

Consider the elastic layer in Fig. 1 with thickness d. Let the coordinate system be chosen so that the x coordinate is parallel and the z coordinate is perpendicular to the layer with the origin a distance b below the layer's bottom surface. Assume the conditions of plane strain and let the waves in the layer be represented in terms of the longitudinal and shear wave potentials ϕ and ψ given by

$$\begin{aligned}\phi &= (\phi' e^{i\alpha z} + \phi'' e^{-i\alpha z}) e^{i(\sigma x - \omega t)},\\ \psi &= (\psi' e^{i\beta z} + \psi'' e^{-i\beta z}) e^{i(\sigma x - \omega t)},\end{aligned} \tag{1}$$

in which ω denotes the frequency and σ is the x component of the wave number. It follows that

$$\sigma = k \sin\theta = \kappa \sin\gamma, \tag{2}$$

where k and κ are the wave numbers for longitudinal and shear wave vectors making acute angles θ and γ, respectively, with the z axis. The z components of the wave vectors, α and β in eqns (1), are defined by

$$\alpha^2 = k^2 - \sigma^2,\ \beta^2 = \kappa^2 - \sigma^2. \tag{3}$$

If v_x, v_z and Z_x, Z_z denote the tangential and normal components of velocity and stress on planes of constant z associated with the wave functions in eqn (1), then, from Brekhovskikh[5], we obtain (omitting the $e^{i(\sigma x - \omega t)}$ factor)

$$\mathbf{f}(z) = \begin{Bmatrix} v_x(z) \\ v_z(z) \\ Z_z(z) \\ Z_x(z) \end{Bmatrix} = \mathbf{T}(z) \begin{Bmatrix} \phi' + \phi'' \\ \phi' - \phi'' \\ \psi' - \psi'' \\ \psi' + \psi'' \end{Bmatrix} = \mathbf{T}(z)\Phi, \tag{4}$$

where T(z) is following 4 by 4 matrix function.

$$\mathbf{T}(z) = \begin{Bmatrix} i\sigma\cos(\alpha z) & -\sigma\sin(\alpha z) & -i\beta\cos(\beta z) & \beta\sin(\beta z) \\ -\alpha\sin(\alpha z) & i\alpha\cos(\alpha z) & -\sigma\sin(\beta z) & i\sigma\cos(\beta z) \\ -i\mu\omega^{-1}(\beta^2-\sigma^2)\cos(\alpha z) & \mu\omega^{-1}(\beta^2-\sigma^2)\sin(\alpha z) & -i2\mu\omega^{-1}\sigma\beta\cos(\beta z) & 2\mu\omega^{-1}\sigma\beta\sin(\beta z) \\ 2\mu\omega^{-1}\alpha\sigma\sin(\alpha z) & -i2\mu\omega^{-1}\alpha\sigma\cos(\alpha z) & \mu\omega^{-1}(\sigma^2-\beta^2)\sin(\beta z) & i\mu\omega^{-1}(\beta^2-\sigma^2)\cos(\beta z) \end{Bmatrix} \tag{5}$$

in which μ is the shear modulus of the elastic layer.

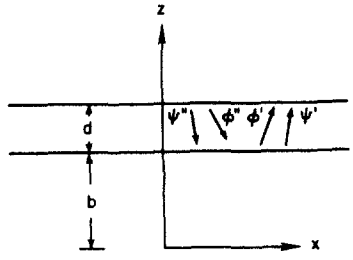

Fig. 1. A single elastic layer containing a system of longitudinal and transverse harmonic plane waves.

When considering waves in multilayered media it is useful to obtain a transfer matrix that relates $\mathbf{f}(z)$ evaluated at the top of a layer to that function evaluated at the bottom of the layer. For the layer in Fig. 1, we obtain from eqn (4)

$$\mathbf{f}(b+d) = \mathbf{T}(b+d)\boldsymbol{\Phi}, \mathbf{f}(b) = \mathbf{T}(b)\boldsymbol{\Phi}. \tag{6}$$

Since the matrix $\mathbf{T}(b)$ is not singular the second of eqn (6) can be solved for $\boldsymbol{\Phi}$, which can then be substituted into the first to yield

$$\mathbf{f}(b+d) = \mathbf{T}(b+d)\mathbf{T}^{-1}(b)\mathbf{f}(b). \tag{7}$$

Thus the matrix $\mathbf{T}(b+d)\mathbf{T}^{-1}(b)$ is the desired transfer matrix.

In Thomson[4] and in the subsequent treatment of Brekhovskikh[5] this transfer matrix was explicitly calculated for the case $b = 0$, i.e. when the bottom of the layer is at $z = 0$. The result was then applied to each layer of a multilayered medium regardless of the location of the layer relative to coordinate system. In order for such a procedure to be valid it is necessary to show that

$$\mathbf{T}(b+d)\mathbf{T}^{-1}(b) = \mathbf{T}(d)\mathbf{T}^{-1}(0) \tag{8}$$

for all b.

The matrix $\mathbf{T}(z)\mathbf{T}^{-1}(z_0)$ is called the propagator matrix and denoted as $P(z, z_0)$ in Gilbert and Backus[11]. The proof of eqn (8) establishes a translation property $P(z, z_0) = P(z - z_0, 0)$ of the propagator matrix in the present application. The formulation in Dunkin[7] is somewhat different from that used here and in [4, 5] and Haskell[12]. In that paper, Dunkin expresses the matrix corresponding to $\mathbf{T}(b+d)\mathbf{T}^{-1}(b)$ in the form $\hat{\mathbf{T}}\mathbf{E}(d)\hat{\mathbf{T}}^{-1}$. Since this form is independent of b, it follows that eqn (8) must be valid. Therefore eqn (7) can be replaced by

$$\mathbf{f}(b+d) = \mathbf{A}(d)\mathbf{f}(b), \tag{9}$$

where

$$\mathbf{A}(d) = \mathbf{T}(d)\mathbf{T}^{-1}(0) \tag{10}$$

is the transfer matrix given by eqn (6.6) of Brekhovshikh[5], if the last row of that matrix is multiplied by 2μ and the last column is divided by 2μ, i.e.

$$\mathbf{A}(d) = \begin{pmatrix} a_{11} & a_{12} & a_{13} & (2\mu)^{-1}a_{14} \\ a_{21} & a_{22} & a_{23} & (2\mu)^{-1}a_{24} \\ a_{31} & a_{32} & a_{33} & (2\mu)^{-1}a_{34} \\ 2\mu a_{41} & 2\mu a_{42} & 2\mu a_{43} & a_{44} \end{pmatrix}, \tag{11}$$

where the elements a_{ij} are given on p. 64 of [5], wherein

$$P = \alpha d, Q = \beta d, b = \sqrt{\mu/\rho}, c = \sqrt{(\lambda + 2\mu)/\rho}, \tag{12}$$

in which λ and ρ are the Lamé constant and density of the elastic layer.

3. REFLECTION COEFFICIENT FOR MULTILAYERED ELASTIC MEDIA

Next consider the structure shown in Fig. 2, which consists of n elastic solid layers of thicknesses $d_1, d_2, \ldots, d_n$ on an elastic half-space. This structure is submerged in a fluid from which a plane longitudinal acoustic wave is incident. The origin of coordinates is located at the interface between the bottom layer and the substrate. In each medium the

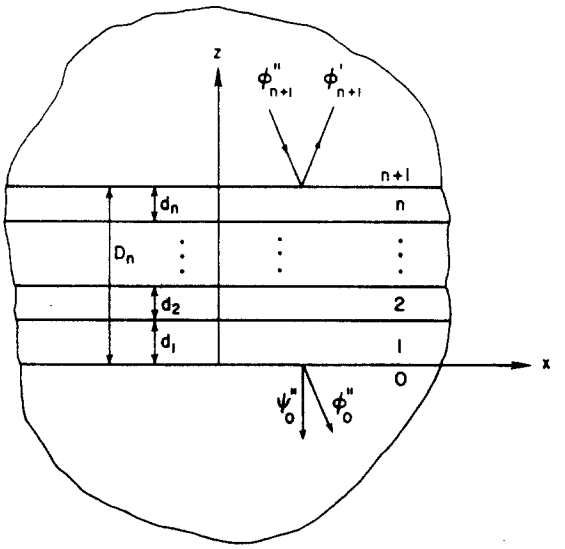

Fig. 2. A halfspace with n elastic layers under a fluid with incident plane acoustic waves.

longitudinal and shear wave potentials have the representation

$$\phi_k = (\phi_k' e^{i\alpha_k z} + \phi_k'' e^{-i\alpha_k z}) e^{i(\sigma x - \omega t)}$$
$$\psi_k = (\psi_k' e^{i\beta_k z} + \psi_k'' e^{-i\beta_k z}) e^{i(\sigma x - \omega t)}, k = 0, 1, 2, \ldots, n+1. \quad (13)$$

Since no shear wave occurs in the fluid, ψ'_{n+1} and ψ''_{n+1} are identically zero. Also ϕ_0' and ψ_0' are zero because only downward traveling waves occur in the substrate. Snell's law is given by

$$\sigma = k_k \sin\theta_k = \kappa_k \sin\gamma_k, k = 0, 1, 2, \ldots, n+1, \quad (14)$$

where k_k and κ_k are the wave numbers for the longitudinal and shear wave vectors making acute angles θ_k and γ_k, respectively, with the z axis. The z components of the wave vectors, α_k and β_k in eqns (13), are defined by

$$\alpha_k^2 = k_k^2 - \sigma^2, \beta_k^2 = \kappa_k^2 - \sigma^2, k = 0, 1, \ldots, n+1. \quad (15)$$

Of course κ_{n+1} and β_{n+1} do not exist since the fluid is assumed to support only longitudinal waves.

Define D_k as the distance from the origin to the top of the kth layer (Fig. 2)

$$D_k = \sum_{j=1}^{k} d_j, D_0 = 0. \quad (16)$$

Then from eqn (9)

$$\mathbf{f}_k(D_k) = \mathbf{A}_k(d_k)\mathbf{f}_k(D_{k-1}). \quad (17)$$

The conditions of continuity of velocity and traction stress components at the layer interfaces is expressed by

$$\mathbf{f}_k(D_{k-1}) = \mathbf{f}_{k-1}(D_{k-1}), \quad (18)$$

so eqns (17) and (18) together yield

$$\mathbf{f}_k(D_k) = \mathbf{A}_k(d_k)\mathbf{A}_{k-1}(d_{k-1}) \ldots \mathbf{A}_1(d_1)\mathbf{f}_0(0). \quad (19)$$

From eqns (4) and (5) and the fact that ϕ_0' and ψ_0' vanish it follows that

$$\mathbf{f}_0(0) = \mathbf{B}\begin{Bmatrix}\phi_0'' \\ \psi_0''\end{Bmatrix} \tag{20}$$

where

$$\mathbf{B} = \begin{pmatrix} i\sigma & i\beta_0 \\ -i\alpha_0 & i\sigma \\ -i\mu_0\omega^{-1}(\beta_0^2 - \sigma^2) & i2\mu_0\omega^{-1}\sigma\beta_0 \\ i2\mu_0\omega^{-1}\alpha_0\sigma & i\mu_0\omega^{-1}(\beta_0^2 - \sigma^2) \end{pmatrix}. \tag{21}$$

From eqns (19)–(21) we obtain

$$\mathbf{f}_n(D_n) = \prod_{j=1}^{n} \mathbf{A}_j(d_j)\mathbf{B}\begin{Bmatrix}\phi_0'' \\ \psi_0''\end{Bmatrix}, \tag{22}$$

in which the matrix product is performed in the order indicated in eqn (19).

It remains only to satisfy the interface condition between the fluid and top layer. Using eqns (4) and (5) and setting μ_{n+1}, ψ_{n+1}'' and ψ_{n+1}' to zero we obtain

$$\begin{Bmatrix} v_z^{n+1}(D_n) \\ Z_z^{n+1}(D_n) \end{Bmatrix} = \begin{pmatrix} \alpha_{n+1} & -\alpha_{n+1} \\ -\lambda_{n+1}k_{n+1}^2\omega^{-1} & -\lambda_{n+1}k_{n+1}^2\omega^{-1} \end{pmatrix} \begin{Bmatrix} i\,e^{iP_{n+1}}\phi_{n+1}' \\ i\,e^{-iP_{n+1}}\phi_{n+1}'' \end{Bmatrix} \tag{23}$$

where

$$P_{n+1} = \alpha_{n+1}D_n. \tag{24}$$

The fluid–solid interface conditions,

$$v_z^{n+1}(D_n) = v_z^n(D_n),\ Z_z^{n+1}(D_n) = Z_z^n(D_n),\ Z_x^{n+1}(D_n) = Z_x^n(D_n) = 0 \tag{25}$$

yield, with use of eqns (22) and (23), the system

$$\begin{aligned} c_{21}^{(n)}\phi_0'' + c_{22}^{(n)}\psi_0'' &= i\alpha_{n+1}\,e^{iP_{n+1}}\phi_{n+1}' - i\alpha_{n+1}\,e^{-iP_{n+1}}\phi_{n+1}'', \\ c_{31}^{(n)}\phi_0'' + c_{32}^{(n)}\psi_0'' &= -i\lambda_{n+1}k_{n+1}^2\omega^{-1}\,e^{iP_{n+1}}\phi_{n+1}' - i\lambda_{n+1}k_{n+1}^2\omega^{-1}\,e^{-iP_{n+1}}\phi_{n+1}'', \\ c_{41}^{(n)}\phi_0'' + c_{42}^{(n)}\psi_0'' &= 0, \end{aligned} \tag{26}$$

in which the 4 by 2 matrix $\mathbf{C}_n$ is defined by

$$\mathbf{C}_n = (c_{ij}^{(n)}) = \prod_{j=1}^{n} \mathbf{A}_j(d_j)\mathbf{B}. \tag{27}$$

The reflection and transmission coefficients are obtained from eqn (26) by solving for the ratios ϕ_{n+1}'/ϕ_{n+1}'', ϕ_0''/ϕ_{n+1}'' and ψ_0''/ϕ_{n+1}''. We will be concerned with only the reflection coefficient, which can be expressed as

$$R = \frac{\phi_{n+1}'}{\phi_{n+1}''} = e^{-i2P_{n+1}}\frac{\Delta_3^{(n)} - Z_{\theta_{n+1}}\Delta_2^{(n)}}{\Delta_3^{(n)} + Z_{\theta_{n+1}}\Delta_2^{(n)}}, \tag{28}$$

where

$$\Delta_i^{(n)} = c_{i1}^{(n)}c_{42}^{(n)} - c_{41}^{(n)}c_{i2}^{(n)},\ i = 2, 3,\ Z_{\theta_{n+1}} = \frac{\rho_{n+1}c_{n+1}}{\cos\theta_{n+1}}, \tag{29}$$

in which c_{n+1} is the acoustic wave speed in the fluid.

The reflection coefficient given by eqns (28) and (29) has the same form as eqn (17) of Bogy and Gracewski[1], which was obtained for a single elastic solid layer on an elastic substrate submerged in a fluid. Indeed the present result reduces for the case $n = 1$ to that obtained in [1].

The result obtained here can also be altered to the case in which the substrate is a fluid. In that case ψ_0'' vanishes and $\mathbf{B}\begin{Bmatrix}\phi_0'' \\ \psi_0''\end{Bmatrix}$ in eqn (21) becomes

$$[i\sigma, -i\alpha_0, -i\omega^{-1}\lambda_0 k_0^2, 0]^T \phi_0''. \tag{30}$$

The first two of eqn (26) provide two equations for the reflection and transmission coefficient and the third requires $c_{41}^{(n)} = 0$ so that $\Delta_i^{(n)} = c_{i1}^{(n)} c_{42}^{(n)}$, $i = 2, 3$. The form of R remains as given in eqn (28), which differs from the corresponding result on p. 66 of [5] by the presence in eqn (28) of the phase term $e^{-i\Omega P_{n+1}}$.

If we define

$$\hat{\phi}_{n+1}' = e^{iP_{n+1}}\phi_{n+1}', \hat{\phi}_{n+1}'' = e^{-iP_{n+1}}\phi_{n+1}'', \tag{31}$$

and also define $\hat{R}$ by

$$\hat{R} = \hat{\phi}_{n+1}'/\hat{\phi}_{n+1}'', \tag{32}$$

then $\hat{R}$ differs from R in eqn (28) by the absence of the phase term. It follows that $|R| = |\hat{R}|$, and therefore the absence of the phase term is not important if the modulus of R is all that is required. However, for applications such as in the calculation of nonspecular reflection of bounded beams the phase of R can be important.

4. NUMERICAL RESULTS FOR TWO LAYERS ON A SOLID SUBSTRATE

In the remainder of this paper we are concerned with a layered structure that has two solid layers on a solid substrate. In particular we consider the structure shown in Fig. 3,

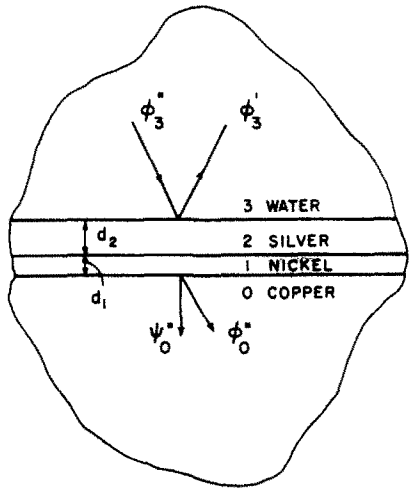

Fig. 3. A copper halfspace with nickel and silver layers under water with incident plane acoustic waves. Material parameters used are listed below:

Material	ρ(gm/cm^3)	c(km/sec)	b(km/sec)
Water	1.0	1.48	—
Silver	10.5	3.60	1.59
Nickel	8.8	5.63	2.96
Copper	8.9	4.70	2.26

which has a copper substrate (material 0) with a nickel layer (material 1) of thickness d_1 and a silver layer (material 2) of thickness d_2. Material 3 is assumed to be water. We wish to investigate the relative effects of different layer thicknesses on the magnitude of the reflection coefficient, the dispersion curve for the lowest leaky Rayleigh mode, and the reflected beam profiles for nonspecular reflection of beams incident at the Rayleigh angle.

From the material parameters given in Fig. 3 it is clear that in the case $d_1 = 0$ a single layer of silver covers copper, which is a "loading" case of Farnell and Adler[3], whereas in the case $d_2 = 0$ a single layer of nickel covers copper, and this is a "stiffening" case of [3]. The reflection coefficient for the single layer case was studied extensively in Bogy and Gracewski[2], which serves as a basis for understanding the results to be presented here for the two layer case.

Reflection coefficient

For a fixed set of materials the reflection coefficient is a function of the incidence angle θ_3 and a frequency–thickness parameter fd_2. Figure 4 presents a study of the dependence of $|R|$ on $\sin\theta_3$. In each of Figs. 4(a–f) the ratio d_1/d_2 of layer thicknesses is fixed and $|R|$ vs $\sin\theta_3$ curves are presented for six values for fd_1 or fd_2 (except in Fig. 4(e) where curves are presented for only five values of fd_2 for reasons to be discussed). In these computations we kept f fixed at 4 MHz and allowed d_2 to take the six values 0, 0.2, 0.4, 0.6, 0.8 and 1.0 mm. As real $\sin\theta_3$ varies from 0 to 1 it follows from eqn (14) that σ varies from 0 to k_3. In the complex σ-plane this is along the real axis from the origin to the value k_3, which is a branch point of the complex function R because of eqn (15). As in [2], we find it instructive here to evaluate $|R|$ along a path slightly below the real axis in the σ-plane. Therefore, for all results in Fig. 4, $|R|$ has been calculated along the path $\sigma = \sigma_R - i0.001$, $0 \leq \sigma_R \leq k_3$, with $\sin\theta_3 = \sigma_R/k_3$. This offset does not noticeably alter $|R|$ from its value along the real axis except near the zeros of R that occur below and close to the real axis, and which are also complex conjugates of poles of R that correspond to leaky Rayleigh modes of interest in connection with nonspecular reflections of bounded beams. Therefore the slight offset provides additional information because the small dips in the $|R|$ curves, which occur in the otherwise flat portions extending to $\sin\theta_3 = 1$, locate the incident Rayleigh angles for the various leaky Rayleigh modes. It should also be noted that in each of Figs. 4(a–f) only the top curve is properly positioned relative to the ordinate scale. The other curves have been shifted downward for clarity and ease of comparison. For each curve $|R| = 1$ in an interval ending at $\sin\theta_3 = 1$.

In Fig. 4(a), $d_1 = 0$ so the structure is water–silver–copper, which is a single layer "loading" case. The results here are qualitatively similar to Fig. 3 of [2], which presents corresponding curves for the loading case of water–brass–stainless steel. In the top curve of Fig. 4(a), $d_2 = 0$ and the reflection coefficient shows the familiar liquid–solid curve[2, 5] for water–copper. The cusp near $\sin\theta_3 = 0.32$ corresponds to the longitudinal wave number of copper, and the kink where $|R|$ again takes the value of unity, near $\sin\theta_3 = 0.66$ corresponds to the shear wave number of copper. The slight dip near $\sin\theta_3 = 0.7$ locates the leaky Rayleigh mode for water–copper. As the thickness d_2 increases the other curves in Fig. 4(a) depict the changes in $|R|$ vs $\sin\theta_3$. Higher leaky Rayleigh modes emerge from the copper shear wave number. This is indicated by the additional slight dips in the right hand portion of the curves. The lowest Rayleigh mode moves toward the silver Rayleigh mode, but the zero that causes the dip in $|R|$ vs $\sin\theta_3$ curve moves too far away from the real axis for the tell-tale dip to be seen. The root locus in the complex σ-plane for this particular mode will be discussed in detail later. The portion of the curves in Fig. 4(a) between the longitudinal and shear wave numbers for copper have a structure that is determined by Lamb-type modes as discussed in Pitts *et al.*[6] and [2]. The sharp down spikes, as seen for example on the $fd_2 = 1.6$ and 3.2 curves, represent zeros of $|R|$ very near the real σ-axis, and they correspond to leaky Lamb-type modes.

In Fig. 4(b), both the silver and nickel layers are present with their thickness ratio fixed at $d_1/d_2 = 0.5$. There are two observable qualitative differences between Fig. 4(a) and Fig. 4(b). In Fig. 4(a) the $|R| = 1$ region remains fixed at the $\sin\theta_3$ values beyond the copper shear wave number. In Fig. 4(b) we see that this region moves toward the shear wave

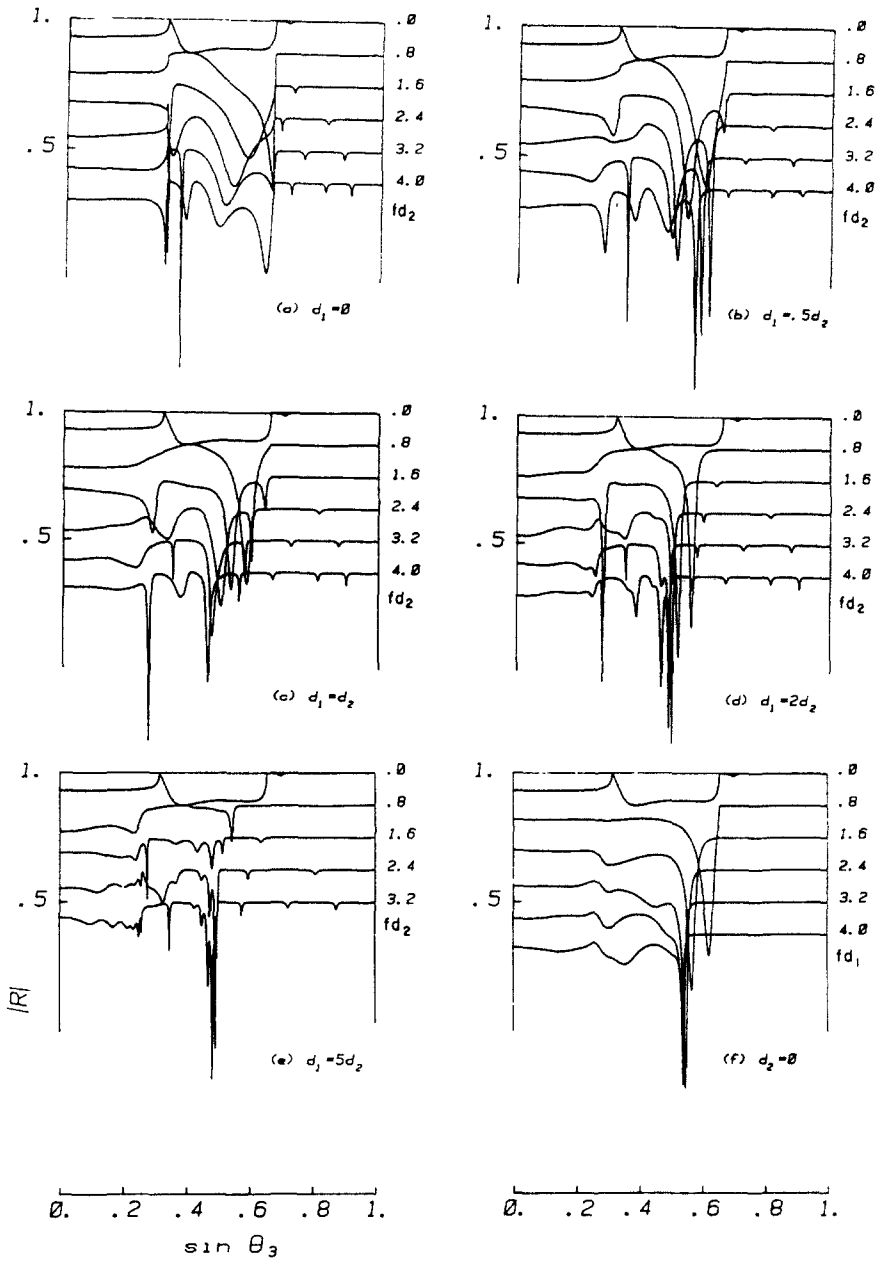

Fig. 4. Dependence of plane wave reflection coefficient on the ratio of layer thicknesses and a frequency-thickness parameter. fd_1 and fd_2 have units of MHz · mm. Only the top curve is properly positioned with respect to the ordinate axis in each graph, i.e. $|R| = 1$ at $\sin\theta_3 = 1$ for all curves. The structure is as shown in Fig. 3.

number for nickel, about $\sin\theta_3 = 0.50$, as d_2 increases. Likewise the mid region, where Lamb-type modes determine the structure, is tending toward the region between the longitudinal and shear wave numbers for nickel. This trend is continued in Fig. 4(c), where the layer thickness ratio is fixed at $d_1/d_2 = 1$. In Figs. 4(d) and 4(e) where $d_1/d_2 = 2$ and 5, respectively, we observe a further continuation of this trend with an increasing amount of small scale structure in the mid, Lamb-mode, regions of the curves, but with very little change in the right hand, Rayleigh-mode, regions. In Fig. 4(e), where $d_1/d_2 = 5$, the $|R|$ vs $\sin\theta_3$ curve is not presented for $fd_2 = 4.0$. This is due to the fact that the accuracy of the computation becomes less as the thickness of the layers increases. Thin layer results can be calculated with single precision, but the thick layer results required double precision. Even double precision was not sufficiently accurate on the IBM-4341 computer to compute the result in Fig. 4(e) for $fd_2 = 4.0$. This accuracy problem is associated with the evaluation

of trigonometric functions at large arguments. A related computational difficulty has been discussed by Dunkin[7] and Schwab and Knopoff[13].

Finally, Fig. 4(f) presents $|R|$ vs $\sin\theta_3$ for $d_2 = 0$, which is the single layer "stiffening" structure of water–nickel–copper. This figure is qualitatively similar to Fig. 4(a–d) of [2], where the structure is water–stainless steel–brass. The top curve, where $d_1 = 0$, again presents the liquid–solid result for water–copper. As predicted in [3], and also seen in [2], an increase in d_1 causes the Rayleigh mode to move to the shear wave number of copper and cut off as a propagating mode. The eventual emergence of the nickel Rayleigh mode as d_1 increases is discussed in detail for the stainless steel on brass structure in [2]. It will also be discussed further here in connection with the pole trajectory analysis to be presented next.

Trajectories of the lowest leaky Rayleigh pole

As indicated earlier the propagating Rayleigh-type interface waves correspond to poles of the reflection coefficient R in eqn (28). These poles are zeros of the denominator $\Delta_3^{(2)} + Z_{\theta_3}\Delta_2^{(2)}$, and they are paired as complex conjugates with zeros of the numerator $\Delta_3^{(2)} - Z_{\theta_3}\Delta_2^{(2)}$. When the fluid is absent Z_{θ_3} vanishes, and the numerator is identical to the denominator. The Rayleigh mode zeros of $\Delta_3^{(2)}$ in this case are real, and the waves propagate without attenuation. When the fluid is present the Rayleigh mode zeros of $\Delta_3^{(2)} + Z_{\theta_3}\Delta_2^{(2)}$ are complex and the attenuation of the leaky Rayleigh wave is given by the imaginary part of the pole.

Figure 5 shows trajectories in the complex σ-plane of the lowest Rayleigh mode pole as d_2 changes at fixed frequency ($f = 4$ MHz) for various fixed ratios of d_1/d_2. The curve for $d_1 = 0$, the single layer loading case of silver on copper, is qualitatively in agreement with the trajectory shown in Fig. 3 of Chimenti *et al.*[8] for the single layer loading case of copper on stainless-steel. It begins, with $d_2 = 0$, at the water–copper Rayleigh pole, $\sigma = 11.9 + i0.17$, and approaches the water–silver Rayleigh pole, $\sigma = 16.4 + i0.53$, as d_2 increases. The four dashed lines in Fig. 5 give an indication of the values of d_2 along the curves. Notice that the magnitude of $\mathrm{Im}(\sigma)$ for the pole (and hence also the conjugate zero) increases to a maximum and then decreases slightly as d_2 increases. The slight dip at the Rayleigh angle in the top curve of Fig. 4(a) corresponds to the conjugate zero for the water–copper Rayleigh pole. It was noted in the discussion of Fig. 4(a) that the dip vanishes as d_2 increases because the zero moves away from the real axis, as seen for the conjugate pole in Fig. 5.

The pole trajectory in Fig. 5 for $d_1 = 0.5d_2$ is similar to that for $d_1 = 0$. The trajectory for $d_1 = d_2$, however, is different for small values of d_2 in that a closed loop occurs. Since the phase speed of the corresponding leaky Rayleigh mode is inversely proportional to the real part of the pole, this loop will lead to a local minimum in the dispersion curve (to be discussed more later with the aid of Fig. 7). The trajectory in Fig. 5 for $d_1 = 2d_2$ does

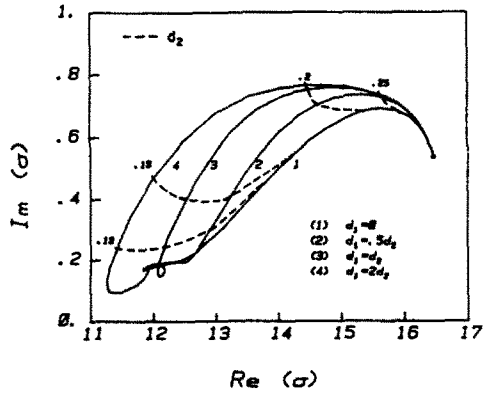

Fig. 5. Trajectories in the complex σ-plane of the lowest Rayleigh mode pole as d_2 (mm) changes, with frequency of 4 MHz and for various ratios of d_1/d_2. The structure is as shown in Fig. 3. $\mathrm{Im}(\beta_0) > 0$.

not have a closed loop but the real part first decreases to a minimum and then increases as d_2 increases.

The pole trajectories for the cases $d_1 = 5d_2$ and $d_2 = 0$ are considerably more complicated than those shown in Fig. 5 and require the separate Fig. 6 for explanation. The difficulty occurs when d_1/d_2 reaches a large enough value such that the trajectories intersect the real axis near $\sigma = 11$. Consider first the case $d_2 = 0$ which is the single layer stiffening case of nickel on copper. The pole trajectory for this case in Fig. 6 is qualitatively similar to Fig. 5 of [2] which gives the corresponding pole trajectory for the single layer stiffening case of stainless steel on copper. The trajectory begins, with $d_2 = 0$, at the water–copper Rayleigh pole and moves to a real value near $\sigma = 11$, which is slightly less than the copper shear wave branch point. According to [3] the Rayleigh mode cuts off at that point and does not propagate for larger values of d_2. As pointed out in [2], however, the water–nickel Rayleigh pole at $\sigma = 9.2 + i0.09$ is approached as d_2 becomes large. This trajectory can be followed backward for decreasing values of d_2. In Fig. 6 there are two sets of pole trajectories for each layered structure that correspond to two different branches of the multivalued function β_0. The trajectory for one branch is drawn with a solid line, that for the other branch is a dashed line. There is also a vertical dashed line which passes through the real shear wave number for copper. To the right of this vertical line the trajectories on the branch $\mathrm{Im}(\beta_0) > 0$ are shown with a solid line and those on the branch $\mathrm{Re}(\beta_0) > 0$ are dashed. To the left of this line the reverse holds, i.e. the $\mathrm{Im}(\beta_0) > 0$ trajectories are dashed and those for $\mathrm{Re}(\beta_0) > 0$ are solid. It is our conjecture, that the solid line trajectories to the right of the vertical dashed line represent the leaky Rayleigh mode pole trajectories that correspond to those shown in Fig. 5 for different ratios of d_1/d_2. If this is the case then the trajectories are discontinuous in the presence of the liquid and the mode does not propagate for d_2 in the range $0.033 < d_2 < 0.135$ mm (i.e. the dashed portion of curve 5 in $\mathrm{Re}(\sigma) < 11.1$) and for $d_1 > 0.13$ mm for $d_2 = 0$. We have observed that in the absence of the liquid all of these trajectories lie on the real axis except the portion that connects the nickel Rayleigh pole to the copper shear wave number, which remains complex between its real end points. Thus in the absence of the liquid the pole trajectories are continuous.

In light of the above discussion the Rayleigh pole trajectory for $d_1 = 5d_2$ in Fig. 6 starts at the water–copper Rayleigh pole at $d_2 = 0$ then decreases to the dashed vertical line near the real axis. It is then discontinuous and starts at a point near $\sigma = 11 + i0.29$, moves to the right and eventually approaches the water–silver Rayleigh pole as d_2 increases.

This root behavior is quite complex, and further information could be obtained to support or discredit our conjecture by experiments and/or calculations of displacement profiles of the type presented in [3].

Dispersion curves for the lowest leaky Rayleigh mode

The pole trajectories shown in Figs. 5 and 6 provide the phase velocities for the corresponding leaky Rayleigh modes. The real part of the pole determines the velocity c

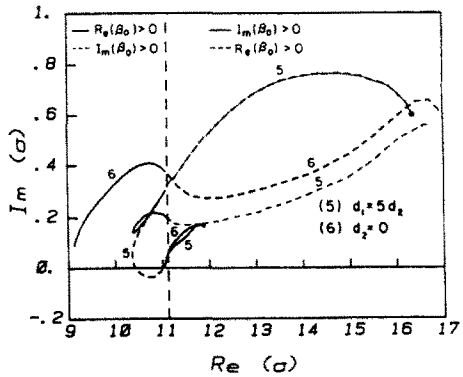

Fig. 6. Trajectories in the complex σ-plane of the lowest Rayleigh mode pole, as d_1 changes. The frequency is 4 MHz and the structure is shown in Fig. 3.

according to

$$c = \omega/\mathrm{Re}\,(\sigma).$$

Figure 7 shows the dispersion curves for the various layer thickness ratios d_1/d_2. Here we plot c vs Q, where Q is the dimensionless quantity defined by

$$Q = \kappa_0 d_2 \text{ (or } Q = \kappa_0 d_1).$$

The curves start for $Q = 0$ at the Rayleigh wave speed for copper and are asymptotic as Q increases to the Rayleigh wave speed of silver. The curves for $d_1 = 0$ and $d_1 = 0.5d_2$ decrease monotonically, but the curves for $d_1 = d_2$ and $d_1 = 2d_2$ have local minima and maxima near $Q = 1$ corresponding to the small loop and section of decreasing magnitude on the trajectories in Fig. 5. The curve for $d_2 = 0$ in Fig. 7 monotonically increases to the copper shear wave speed where the mode cuts off. Finally, the curve for $d_1 = 5d_2$ has a dashed portion that corresponds to the dashed portion of curve 5 in Fig. 6 in the region $\mathrm{Re}\,(\sigma) < 11.1$. The propagation of waves with such speeds remains in question.

Nonspecular reflection of bounded beams in fluid

The phenomenon of nonspecular reflection of bounded acoustic beams incident from the fluid at a Rayleigh angle on the liquid–solid and the liquid–solid–liquid (single elastic layer in fluid) structures has been discussed in [9, 10]. In Bertoni and Tamir[9] the phenomenon is thoroughly explained in the context of the liquid–solid structure. The explanation was extended to the liquid–solid–liquid structure in Pitts *et al.*[10]. The basic phenomenon and its mathematical representation are independent of the type of layered structure. If the incident beam is near a Rayleigh angle (i.e. $\sin\theta_3$ has the value corresponding to one of the slight dips in the right portions of Figs. 4a–f) it excites the leaky Rayleigh mode so that only part of the beam energy is specularly reflected and the other part begins to propagate as the leaky Rayleigh wave. This mode leaks its energy back into the liquid as a wave that propagates away from the structure at the same angle as the specularly reflected part. The sum of these two reflected and reradiated parts combine to give the nonspecularly reflected beam. In [9] the incident bounded beam was represented as a Fourier integral of plane waves over all wave numbers. The incident beam profile is assumed to be a Gaussian function, which gives a simple Fourier transform. The reflected beam is a similar Fourier integral, but contains the reflection coefficient R as a factor in the integrand. The integrals for the reflected profiles can either be evaluated numerically using the entire reflection coefficient or the reflection coefficient can be approximated in the neighborhood of the Rayleigh angle in terms of its poles and zeros. Two basic types of nonspecularly reflected profiles have been identified, depending on the type of pole-zero pair that determines the leaky mode. These were identified in Pitts *et al.*[10] as

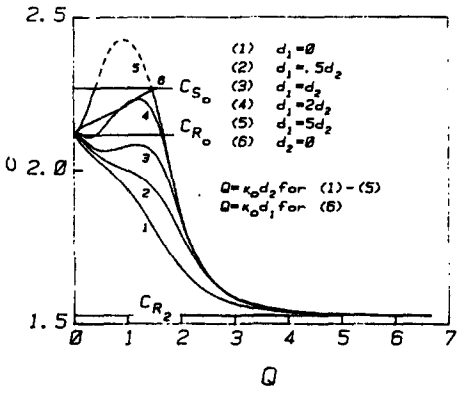

Fig. 7. Dispersion curves showing lowest Rayleigh mode phase speed as a function of the dimensionless parameter Q.

Rayleigh-type, where the pole-zero pair are complex conjugates, and as Lamb–type, where the zero is real and the pole is complex with the same real part as the zero and with a positive imaginary part. Approximations for the reflected beam were developed for both types of modes. (We have observed in [2], where the structure is a layered half-space, that modes can also occur which are neither Rayleigh or Lamb type.)

It has been found in [10] that the reflected beam profiles for both the Rayleigh and Lamb-type modes depend on the half beam width projection w_0 and the imaginary part of the pole σ_I through the parameter h defined by

$$h = w_0\sigma_I. \tag{33}$$

In the present paper we restrict the study of nonspecularly reflected beam profiles to those of the Rayleigh-type and as determined by the lowest Rayleigh modes whose pole trajectories are shown in Figs. 5 and 6. The profile computations were made according to eqn (8) of [10] using the reflection coefficient presented here in eqn (28).

Figure 8 shows an incident Gaussian beam profile (dashed curve) with $w_0 = 2.67$ mm and several reflected beam profiles that correspond to the Rayleigh poles in Fig. 5 on the trajectory for the case $d_1 = d_2 = d$. The particular values of d chosen are $d = 0.1$, 0.125, 0.15, 0.175 and 0.2 mm, which give values of $\sigma_I = 0.156$, 0.218, 0.397, 0.652, and 0.749 $(\text{mm})^{-1}$, so that the values of h in eqn (33) are $h = 0.416$, 0.583, 1.06, 1.74 and 2.0, respectively. The profiles in Fig. 8 agree with the Rayleigh type profiles in Fig. 6 of [10] in cases where the same values of h can be identified, even though the reflection coefficient is different.

Figure 9 shows reflected beam profiles corresponding to the Rayleigh poles obtained from Figs. 5 and 6 along the dashed line for $d_2 = 0.15$ mm and for the ratios $d_1/d_2 = 0$, 0.5, 1, 2 and 5. The values of σ_I are 0.547, 0.404, 0.397, 0.468 and 0.509 $(\text{mm})^{-1}$, giving values of $h = 1.46$, 1.08, 1.06, 1.25 and 1.36, respectively. Of course the incident angle θ_3 has to be adjusted to correspond to $\sigma_R = k_3 \sin\theta_3$. The similarity of these profiles results from the closeness of the imaginary parts σ_I.

5. DISCUSSION AND CONCLUSIONS

In Section 2 we established the result in eqn (8), which had previously been assumed in [4, 5] without proof or discussion. This result is important, since it leads to significant simplification in the derivation of and the expression for the reflection coefficient for multi-layered media. Such a reflection coefficient was derived in Section 3, and the result obtained in eqn (28) differs in its phase from the corresponding expression presented in [4, 5]. This difference is unimportant if the reflection coefficient amplitude is the only thing

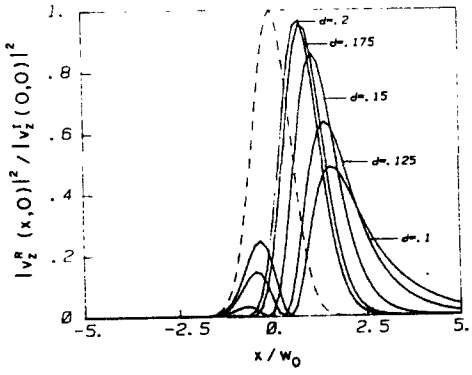

Fig. 8. Reflected beam profile intensities corresponding to bounded beams with half width projection w_0 incident at the Rayleigh angle, as determined by points on curve 3 of Fig. 5 for the indicated equal layer thickness d(mm). The frequency is 4 MHz and the structure is shown in Fig. 3. The dashed line is the incident Gaussian beam.

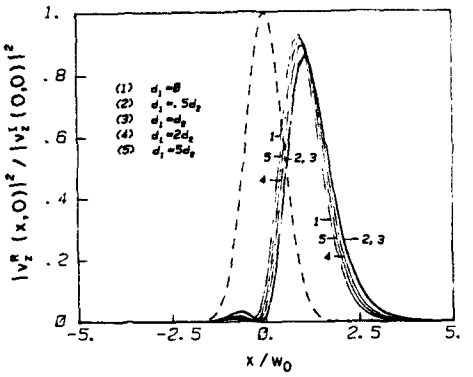

Fig. 9. Same as Fig. 8 except poles are determined by the values $d_2 = 0.15$ mm in Figs. 5 and 6 for different thickness ratios.

desired. However, the phase of the nonspecularly reflected beam is also affected by the phase of the reflection coefficient, and this may be important in some applications.

In Section 4 the particular layered structure in Fig. 3 was studied. Numerical computations of $|R|$ were presented graphically for various values of layer thicknesses. The structure chosen for study, i.e. silver and nickel layers on a copper substrate, has the property of a single layer "loaded" halfspace when the nickel layer vanishes and the silver layer remains. It has the property of a "stiffened" halfspace when the silver layer vanishes and the nickel layer remains. These special cases were studied previously in [2], but with different materials. The computation of the results presented in Fig. 4 incurred some difficulties as the layer thicknesses increased. In particular the $fd_2 = 4.0$ curve for Fig. 4(e) could not be calculated with sufficient accuracy using our numerial technique. Further work needs to be done to remove this difficulty, which is associated with the evaluation of trigonometric functions at large arguments.

The study of nonspecular reflection of bounded beams incident in the fluid at the Rayleigh angle requires the location of the pole-zero pairs associated with the propagating Rayleigh modes. These Rayleigh modes appear in increasing number in the layered structure as the frequency–thickness parameter increases. We concentrated on the lowest such mode and presented in Figs. 5 and 6 trajectories of the pole in the complex wave number plane, corresponding to changing layer thicknesses. There are several multivalued functions in the reflection coefficient that result from the α_k and β_k defined in eqn (15). A particular choice of branches leads to a particular set of pole trajectories and therefore determines the predicted propagating modes. It also determines the reflection coefficient. The corresponding branch point κ_0, associated with the shear wave speed of the copper substrate, occurs in Figs. 5 and 6 at about $\sigma = 11.1 + i0$. This is the cause of the complexity that appears in Fig. 6. Here the trajectory crosses into the region $\mathrm{Re}(\sigma) < \kappa_0$, the branch is chosen according to $\mathrm{Re}(\beta_0) > 0$, and the shear wave in the substrate propagates away from the layers, leading to a leakage of the energy into the substrate. For thick enough layers, so that on curve 6 in Fig. 6 the trajectory value of $\mathrm{Re}(\sigma)$ approaches the nickel Rayleigh pole, near $\mathrm{Re}(\sigma) = 9.2\ (\mathrm{mm})^{-1}$, negligible wave energy reaches the nickel–copper interface and so the leaky substrate problem does not arise. However, in the neighborhood of $\mathrm{Re}(\sigma) = \kappa_0^-$ the substrate leakage is significant, and the Rayleigh type modes do not propagate.

The dispersion curves in Fig. 7 show some interesting properties as the layer thickness ratios change. The curves are drawn as solid lines when the phase speed is less than the shear wave speed c_{s_0} of the copper substrate. The dashed part of curve 5 indicates our reluctance to speak of the mode as propagating in this region. The maximum and minimum in curve 4 could possibly be of interest in the design of signal processing devices.

The nonspecularly reflected beam profiles presented in Figs. 8 and 9 are very similar to previously known results in [9, 10], given the root values of $\mathrm{Im}(\sigma)$ and the beam width parameter w_0. We experienced a difficulty with the computation of the reflected beam profiles for conditions in Fig. 5 when the pole occurs in neighborhood of the silver

Rayleigh pole, $\sigma \simeq 16.4 + i0.53$. This difficulty arises because the fluid acoustic wave branch point k_3 occurs at $16.9 + i0$, and the meaning of the reflection coefficient, which appears in the Fourier integral representation of the reflected beam profile in eqn (8) of [10], is unclear for $\mathrm{Re}(\sigma) > k_3$. A simple disregard for this difficulty leads to obviously incorrect results for the reflected beam profiles. The different branch choice for α_3 produced unfamiliar reflected beam profiles in which we had little confidence. Further work needs to be done on the integral representation and its computation in this region. This problem is even more apparent if one uses gold in place of silver for the top layer. This is because the Rayleigh wave number for gold is greater than k_3. Evidently the Rayleigh wave in gold cannot be excited by acoustic waves in water.

Acknowledgements—This research was partially supported by the National Science Foundation under Grant CME-8017840 and by Lawrence Livermore Laboratory Purchase Order No. 7734501 to the University of California, Berkeley. One of us, S. M. G., would like to acknowledge support by an IBM Predoctoral Fellowship. We are grateful to Prof. A. K. Mal for bringing our attention to [7, 13].

REFERENCES

1. D. B. Bogy and S. M. Gracewski, Reflection coefficient for plane waves in a fluid incident on a layered elastic half-space. *J. Appl. Mech.* **50**, 405–414 (1983).
2. D. B. Bogy and S. M. Gracewski, On the plane wave reflection coefficient and nonspecular reflection of bounded beams for layered half spaces under water. *J. Acoust. Soc. Am.* **74**, 591–599 (1983).
3. G. W. Farnell and E. L. Adler, Elastic wave propagation in thin layers. In *Physical Acoustics*, Vol. 9, pp. 35–127. Academic Press, New York (1972).
4. W. T. Thomson, Transmission of elastic waves through a stratified solid medium. *J. Appl. Phys.* **21**, 89 (1950).
5. L. M. Brekhovskikh, *Waves in Layered Media*. Academic Press, New York (1960).
6. L. E. Pitts, T. J. Plona and W. G. Mayer, Theoretical similarities of Rayleigh and Lamb modes of vibration. *J. Acoust. Soc. Am.* **60**, 374–377 (1976).
7. J. W. Dunkin, Computation of modal solutions in layered, elastic media at high frequencies. *Bull. Seism. Soc. Am.* **55**, 335–358 (1965).
8. D. E. Chimenti, A. H. Nayfeh and D. L. Butler, Leaky Rayleigh waves on a layered halfspace. *J. Appl. Phys.* **53**, 170–176 (1982).
9. H. L. Bertoni and T. Tamir, Unified theory of Rayleigh-angle phenomena for acoustic beams at liquid–solid interfaces. *Appl. Phys.* **2**, 157–172 (1973).
10. L. E. Pitts, T. J. Plona and W. G. Mayer, Theory of nonspecular reflection effects for an ultrasonic beam incident on a solid plate in a liquid. *IEEE Trans. Sonics and Ultrasonics* **SU-24**, 101–109 (1977).
11. F. Gilbert and G. E. Backus, Propagator matrices in elastic wave and vibration problems. *Geophysics* **31**, 326–332 (1966).
12. N. A. Haskell, Dispersion of surface waves on multilayered media. *Bull. Seism. Soc. Am.* **43**, 17–34 (1953).
13. F. Schwab and L. Knopoff, Surface-wave dispersion computations. *Bull Seism. Soc. Am.* **60**, 321–344 (1970).